ADVANCED FUNCTIONAL MATERIALS
www.afm-journal.de

Synthetic Crystals of Silver with Carbon: 3D Epitaxy of Carbon Nanostructures in the Silver Lattice

Lourdes G. Salamanca-Riba, Romaine A. Isaacs, Melburne C. LeMieux, Jiayu Wan, Karen Gaskell, Yeping Jiang, Manfred Wuttig, Azzam N. Mansour, Sergey N. Rashkeev, Maija M. Kuklja, Peter Y. Zavalij, Jaime R. Santiago, and Liangbing Hu*

Only minimum amounts of carbon can be incorporated into silver, gold, and copper in a thermodynamically stable form. Here, the structure of stable silver carbon alloys is described, which are produced by thermoelectrically charging molten silver with carbon ions. Transmission electron microscopy and Raman scattering are combined to establish that large amount of carbon is accommodated in the form of epitaxial graphene-like sheets. The carbon bonds covalently to the silver matrix as predicted from density functional theory (DFT) calculations with bond energies in the range 1.1–2.2 eV per atom or vacancy. Graphitic-like sheets embedded in the crystal lattice of silver form 3D epitaxial structures with the host metal with a strain of ≈13% compared to equilibrium graphene. The carbon nanostructures persist upon remelting and resolidification. A DFT-based analysis of the phonon density of states confirms the presence of intense vibration modes related to the Ag—C bonds observed in the Raman spectra of the alloy. The solid silver–high carbon alloy, termed "Ag-covetic," displays room temperature electrical conductivity of 5.62×10^7 S m^{-1} even for carbon concentrations of up to ≈6 wt% (36 at%). This process of incorporation of carbon presents a new paradigm for electrocharging assisted bulk processing.

1. Introduction

Noble metals, such as silver, gold, platinum, and palladium, are widely used in many applications due to their high electrical conductivities, high resistance to oxidation and their high malleability. Silver, for example, has the highest ambient electrical (6.3×10^7 S m^{-1}) and thermal (420 W m^{-1} K^{-1}) conductivities of all metals. Copper is more abundant than noble metals and more economical. It also has high electrical and thermal conductivities. Silver and copper are commonly used in components from consumer electronics to jewelry. However, their practical use and lifetime are limited, or governed by costly maintenance steps, because of their propensity to oxidize or corrode under atmospheric conditions. This is a critical downside in existing applications, as well as a limitation for advanced new applications that require these materials in nanoscale where limited instances of corrosion and/or migration can severely diminish device performance. Cu forms non conducting CuO or Cu_2O when exposed to the environment. Ag tarnishes by reacting with sulfur[1] and creating a nonconducting layer of Ag_2S on the surface of the material, particularly detrimental in nanoscale structures of Ag.[2,3]

Carbon on the other hand—an essential element in soft and hard materials—is commonly used in macroscale applications ranging from structural reinforcement (steel, carbon, fiber), high end thermal management (diamond) and many more, as well as nanoscale applications including advanced electronics (buckyballs, carbon nanotubes (CNTs), and graphene) for its high-strength, excellent thermal/electrical conductivities, and corrosion resistance. Considering macroscale processes, besides iron, it has not been possible to introduce C into metals such as Ag, Au, and Cu in a stable form and in concentrations larger than ppm levels. Carbon has almost no solubility in these metals as shown by their corresponding C–M (M = Ag, Au, and Cu) binary phase diagrams.[4] It is the essential alloying element in steel where it forms stable carbides and enhances steel's resistance to oxidation. Silver forms metastable carbide Ag_2C_2, called silver acetylide, which is a heat and shock sensitive white powder

Prof. L. G. Salamanca-Riba, R. A. Isaacs,
Dr. M. C. LeMieux, J. Wan, Prof. M. Wuttig,
Dr. S. N. Rashkeev, Dr. M. Kuklja, Assist. Prof. L. Hu
Materials Science and Engineering Department
University of Maryland
College Park, MD 20742, USA
E-mail: riba@umd.edu
Dr. K. Gaskell, Dr. P. Y. Zavalij
Department of Chemistry and Biochemistry
University of Maryland
College Park, MD 20742, USA
Dr. Y. Jiang
Department of Physics
University of Maryland
College Park, MD 20742, USA
Dr. A. N. Mansour, Dr. J. R. Santiago
Naval Surface Warfare Center
Carderock Division
West Bethesda, MD 20817, USA
Dr. S. N. Rashkeev
Qatar Foundation
Qatar Environment and Energy Research Institute
P. O. Box 5825, Doha, Qatar

DOI: 10.1002/adfm.201501156

used as explosive in detonators. However, attempts to incorporate C in the bulk structure of silver and copper in a stable form to improve their oxidation resistance, mechanical strength, and electrical properties have only been recently reported for Cu[5] using the same method as reported here for Ag.

Considering nanoscale processes, graphene[6] and CNTs[7] are two forms of carbon that are also being considered in nanoelectronics because of their high electrical and thermal conductivities. Even though, both graphene and CNTs can now be fabricated with fairly high degree of perfection and control using exfoliation,[6] chemical vapor deposition (CVD),[8] SiC desorption,[9] arc discharge evaporation,[7] etc., they are still not easy to synthesize in large quantities to be used in nanoelectronics.[2,6,8,9] Chemical oxidation of graphite can give rise to reduced graphene oxide,[10] and shear exfoliation in liquids[11] largely produces graphene flakes. Thus, a great amount of research is now directed toward combining metals such as silver and copper (nanowires or thin films) with nanocarbons including graphene[12] and CNTs.[13,14] For example, graphene incorporated in copper in a layered nanostructure exhibits a large increase in the mechanical properties of copper.[15] CNT-copper composite structures display conductivity similar to copper with 100-fold increase in current carrying capacity.[14] However, these processes require several deposition steps to form a sandwich or layering structure. More importantly, the carbon and metal phases are not strongly (chemically) bound to each other. A one-step mixing process of carbon—especially nanocarbons—with silver and copper with strong bonding between carbon/metal phases will be beneficial for materials across all length scales. Electrocharging assisted bulk processing consisting of the application of a high current to a mixture of molten metal and activated carbon particles as presented in this paper satisfies this requirement. Carbon integrated into the lattice of these important metals is expected to increase the metals' resistance to tarnishing (silver) and oxidation (copper) which is a big concern in nanoelectronics, the mechanical strength and ampacity among other properties.

Our goal has been to solve this fundamental issue of strong carbon/metal bonding in silver and copper through a unique class of materials called "covetics" which are prepared using electrocharging assisted bulk processing method.[16] In this work, we aim to explore the incorporation of C in silver (so-called, Ag covetic), investigate if and to what extent the C exists in the form of nanocarbon structures, including nanocrystalline graphite and graphene. Our report represents not only an innovative way to introduce nanocarbon into silver but also the formation of 3D nanoepitaxy of the nanocarbons with respect to the host lattice by an electrodoping technique. This new method of incorporating carbon in a metal is expected to be successful in any metal and has recently been reported for copper.[5] We are investigating carbon incorporation in silver, copper, and aluminum and demonstrate a 3D epitaxial form of graphitic carbon in silver covetic.

2. Incorporation of C in Silver

Carbon with nominal concentrations of 3 and 6 wt% (21.7 and 36.4 at%, respectively) was introduced in 99.99% silver by adding 20–50 μm particles of activated carbon and stirring the liquid metal to induce incorporation of the C in the metal while simultaneously applying a high DC current above a critical current below which no covetic is formed. We believe that the critical current is required to create ionization of the carbon so that the silver melt is in equilibrium with carbon ions instead of carbon atoms. While we do not know how the carbon ions migrate into the silver, a likely mechanism is electromigration.[17] We believe that the high power used (I = 130 A, V = 30–40 V, P = 3900–5200 J s^{-1}) creates an arc discharge in the melt giving rise to increase in temperature of the metal high enough to induce chemical reactions and processes in the liquid metal. This would create ions, both in the metal and the activated carbon particles, and electrons that can react and bond to each other. Arc discharges have been created in liquids to grow CNT[18] and carbon nano-onions[19] by underwater arc discharge methods. We are currently investigating the mechanism of C incorporation in covetics. The mode of incorporation will be discussed in a sequel paper. This manuscript focuses on identifying the presence and form of carbon in silver covetics, and finding evidence of bonding between C and Ag. The samples with nominal 3 and 6 wt% C in silver covetic are denoted Ag cv 3% and Ag cv 6%, respectively.

2.1. Carbon Distribution in Silver

In order to characterize the distribution of C in the Ag covetics we performed X-ray photoelectron spectroscopy (XPS) depth profiles. The profile from an Ag cv 3% sample in **Figure 1**a shows C concentration with depth of ≈8 at% (≈1.0 wt%) after 1 min of sputtering with Ar ions indicating that the C distribution is fairly uniform in the bulk after the top layer of hydrocarbon contamination has been removed. This trend continued up to a sputtering time of 33 min. These data are compared to equivalent spectra obtained at the same time from an Ag foil (0% C) in Figure 1b which shows C contamination at the surface and 0% C and 0% O after 1 min of sputtering. Even though the C content in the covetic samples is less than the nominal C concentration of 3 wt%, the spectra indicate that C is incorporated in the bulk of the Ag covetic sample in much larger concentrations than expected from the Ag—C binary phase diagram which is ≈4×10^{-3} wt% at ≈1500 K.

The basic metal lattice structure of the Ag covetic does not change with the incorporation of C as measured by X-ray diffraction (XRD) from the Ag cv 6% sample (Figure S1, Supporting Information) but the lattice expands by 0.05%. The average isotropic grain size is very small, 70 nm, and, despite cubic symmetry, the sample shows substantial <111> texture. No peaks indicating graphite or any other allotrope of carbon were observed in the XRD spectrum. A comparison of the L_3-edge X-ray absorption near edge structure (XANES) data and Fourier transforms of k^3-weighted extended X-ray absorption fine structure (EXAFS) spectra for Ag covetic and an Ag foil displayed in Figure S2, Supporting Information, demonstrate that the C does not affect the bulk electronic and atomic structure of silver.

2.2. 3D Epitaxy of Carbon Nanostructures with the Silver Lattice

The mode of C incorporation in Ag covetic is observed directly in the TEM images and diffraction patterns presented in

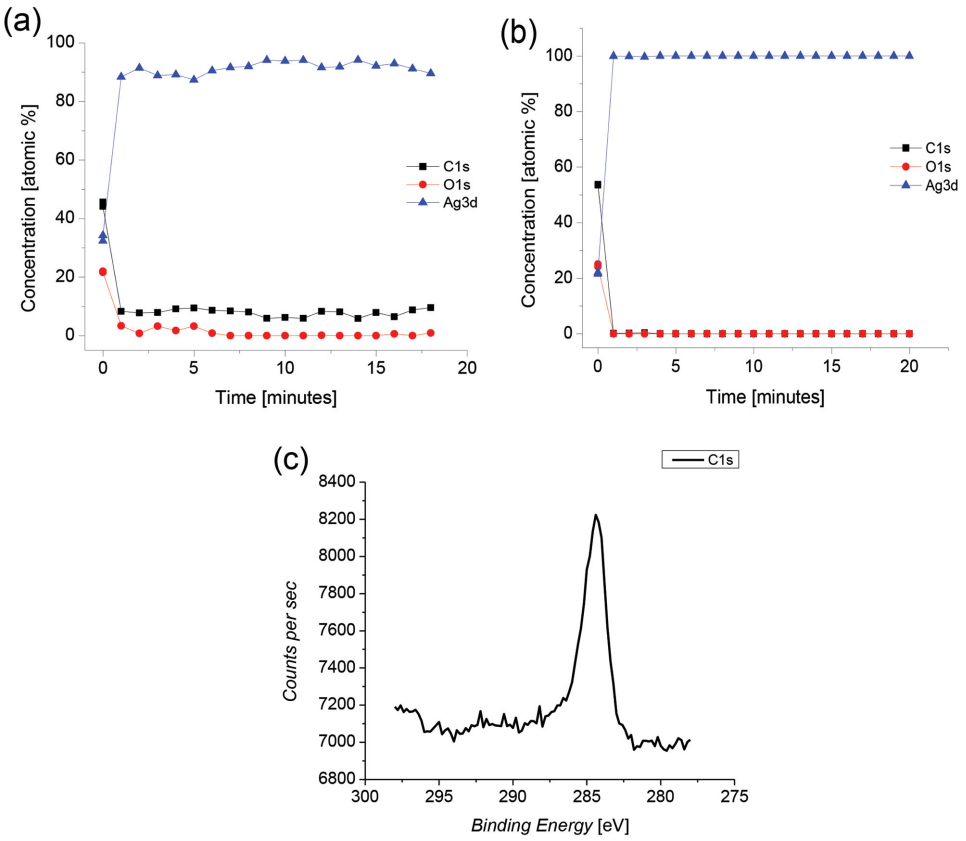

Figure 1. XPS depth profiles from a) Ag cv 3% and b) Ag foil. The C 1s signal decreases after 1 min of sputtering and levels out at ≈8 at% in (a) and 0% in (b). The C concentration in (a) oscillates from ≈6 at% to ≈10 at%, (≈0.7 to 1.2 wt% C). Oxygen contamination is seen at the surface in (a) and (b) but decreases to 0% after 1 min of sputtering. c) C 1s spectrum from an Ag cv 6% sample after sputtering for 360 s with asymmetric shape. The long tail in the high energy range of the peak in (c) is characteristic of C with sp^2 bonding.

Figure 2. The electron diffraction pattern in Figure 2a shows overlap of the (111) zone axis from Ag (strong spots) with additional weak spots (marked with arrows) that do not correspond to Ag. These weak spots form a hexagonal array and lie between the <220> Ag spots. The interplanar distances obtained from the weak spots closest to the transmitted beam are 0.244 ± 0.004 nm which do not correspond to any Ag interplanar distance. We compare this distance to possible interplanar distances of Ag_2S, the compound that forms when silver tarnishes. There are two structures reported for Ag_2S; the room temperature monoclinic phase, Acanthite,[20] with $a = 0.423$, $b = 0.691$, and $c = 0.786$ nm, and $\beta = 99.58°$, and a high temperature phase of Ag_2S observed above ≈176° C. The high temperature phase is a body center cubic structure called Argentite with $a = 0.489$ nm.[21] Details of this analysis are given in the Supporting Information; in summary, we find no diffraction pattern in either structure characteristic of a hexagonal symmetry as the one in Figure 2a. The closest pattern is the $(6\bar{3}1)$ in the Acanthite phase which is pseudo-hexagonal as presented in the schematic of Figure S3, Supporting Information. It is unlikely for Ag_2S to form a distorted structure epitaxially on the (111) plane of Ag with ≈8% strain. Furthermore, our electron energy loss spectra (EELS) obtained from this region of the sample did not show any appreciable signal for S. Instead, EELS indicates that besides Ag there is only C present in the area. Thus, we compare the weak spot pattern in Figure 2a to the (0001) electron diffraction pattern of graphite which is hexagonal. However, the $\langle 10\bar{1}0 \rangle$ interplanar distance in graphite is 0.2127 nm which differs from the measured interplanar distance of 0.244 nm by ≈13%. Single and double layer graphene are remarkably elastic and have been shown to stretch isotropically by up to ≈20%.[22] Hence, it is possible that the carbon in Ag covetic forms layers of graphitic-like carbon which is under ≈13% tensile strain. This enormous strain is surprising because graphene has been reported to have a negative thermal expansion coefficient (TEC) from 200 to 400 K with a room temperature value of $-8 \pm 0.7 \times 10^{-6}$ K^{-1}[23] although other reports indicate a negative TEC which changes to a positive value between 300 and 400 K.[24] A more recent report estimates a positive TEC from room temperature up to 800 K based on the Raman shift of the G peak with temperature.[25] As mentioned by Linas et al.[25] the substrate supporting the graphene plays a very important role in the expansion of graphene. In the case of covetics, the "substrate" is silver which has a TEC of $\approx 1.9 \times 10^{-5}$ K^{-1}. There are two contributions to the strain in the graphitic layer in silver covetic: one due to lattice mismatch at a temperature just below the melting point of silver, and one due to mismatch in the TECs of graphene and silver. Once the material starts to solidify during carbon incorporation in the covetics process, the Ag would have a lattice constant of ≈0.4186 nm (at $T \approx 1200$ K).

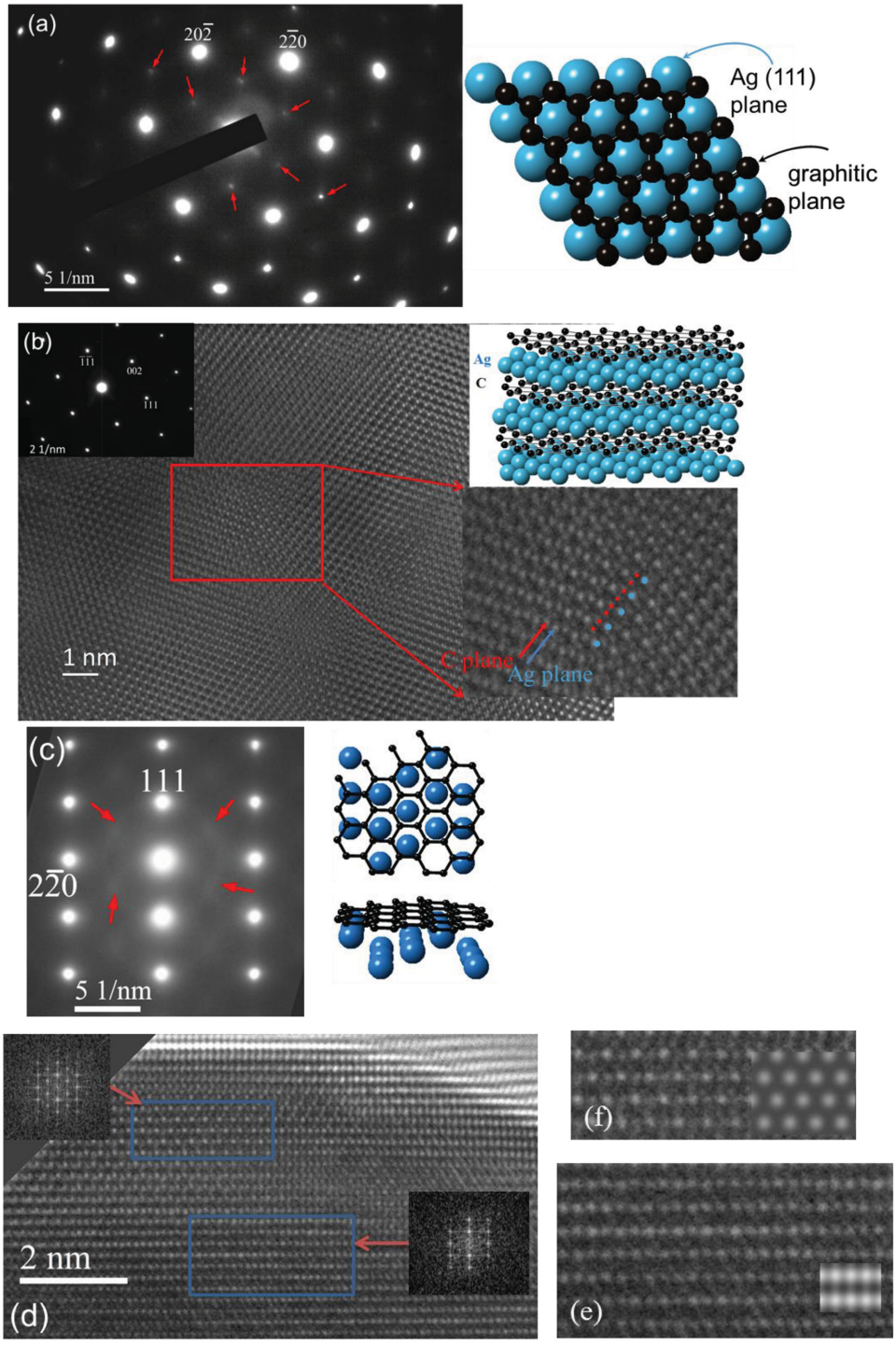

Figure 2. a) (111) electron diffraction pattern from Ag covetic 3% (strong spots are <220> Ag) with (0001) graphite-like diffraction pattern (weak spots marked with red arrows) showing 3D epitaxy between Ag and graphitic-like sheets. The schematic on the right presents the epitaxial orientation between the (111) atomic plane of Ag (blue) and the (0001) plane of graphite (black). b) $(1\bar{1}0)$ HRTEM image and corresponding diffraction pattern from an Ag cv 3% sample. The schematic in (b) shows a model of the structure observed in the image (blue dots are Ag atoms, black dots are C atoms) corresponding to the diffraction pattern in (a). c) $[11\bar{2}]$ electron diffraction pattern from an Ag cv 3% sample. The broad spots marked by arrows agree with the $\langle 10\bar{1}0 \rangle$ reciprocal lattice vectors from graphite. d) $(11\bar{2})$ HRTEM image of Ag cv 3% sample from the same area as (c). The insets in (d) are FFT from the corresponding regions in the blue rectangles. Higher magnification images of (e) the bottom rectangle and (f) top rectangle in (d) with inset computer image simulations for Ag $(11\bar{2})$ (for a sample thickness of 2.25 nm and Scherzer focus $\Delta f = -43.4$ nm) and graphene (0001) (for a sample thickness of one monolayer and Scherzer focus), respectively. The schematics in (c) present the graphene (black) and Ag (blue) with the orientation observed in the diffraction pattern (c) and the image in (d) top (top view) bottom (side view).

At this temperature single and double layer graphene have a lattice constant of ≈0.24565 and ≈0.24595 nm, respectively.[26] The mismatch between the low potential sites in Ag of 0.1669 nm, and the C—C interatomic distance in graphene at this temperature would be ≈17% for single layer graphene and ≈16.9% for double layer graphene. At room temperature, however, the mismatch is slightly reduced to ≈15% for both single and double layer graphene. Thus, it is conceivable that the high strain in Ag covetic results from epitaxial accommodation of the graphitic layers and the metal lattice. Such a high strain could only be possible if the graphitic regions are very thin; only one or two atomic layers thick, which is consistent with the weak and broad graphitic spots in Figure 2a and could give rise to interesting properties of this alloy. The relative orientation between the graphitic spots and the Ag spots in Figure 2a indicates a 3D preferred orientation of the graphitic-like sheets with Ag in an epitaxial relation of (111) Ag//(0001) graphite and <110> Ag//<$11\bar{2}0$> graphite as shown in the schematic in Figure 2a.

More detail of the relative orientation between the graphitic-like layers and Ag can be observed in Figure 2b which shows a high resolution TEM (HRTEM) image of Ag cv 3% where there seem to be regions of ≈3–5 nm containing alternating graphene-like planes and Ag (111) planes (magnified image). Intensity scans along consecutive (111) planes show maxima corresponding to the separation between Ag atoms in the (111) plane (blue dots) and between C atoms in graphene (red dots). This configuration agrees with the diffraction pattern in Figure 2a and is not surprising since the (111) plane in fcc (face-centered cubic) materials has hexagonal symmetry and, therefore, is a preferred plane for graphene although the ≈15% mismatch between the interstitial sites in Ag (111) and the C—C interatomic distance (0.142 nm) in graphene is very large. However, the graphitic regions with the large strain are very small of ≈3–5 nm. The Ag–Ag interplanar distance normal to the alternating Ag/graphene planes in this area increases by ≈0.6% in order to accommodate the graphitic planes. The schematic in Figure 2b is a model structure for this area in which the C atoms sit at the interstitial tetrahedral sites of the Ag lattice.

Other regions of the sample displayed different orientations of the graphitic-like sheets with respect to the Ag lattice and under less strain. One example is observed in the electron diffraction pattern in Figure 2c which corresponds to the $(11\bar{2})$ zone axis of silver and indicates the tetragonal symmetry as expected along this crystallographic direction. The intentional overexposure reveals a weak ring and broad spots (marked by arrows) which correspond to graphite-like $\langle 10\bar{1}0 \rangle$ reciprocal lattice vectors similar to the diffraction pattern in Figure 2a. Again, the position of the broad spots does not correspond to any allowed reflection of Ag. Rather, they point toward small semidisordered regions of graphite-like structure in the silver lattice. These structures can be seen in the HRTEM taken from the same area, Figure 2d. They display hexagonal symmetry in the upper part of the figure (top blue rectangle) and rectangular symmetry of the bottom part as can be confirmed by the corresponding fast Fourier transforms (FFT) presented as insets to the image. The region of hexagonal symmetry corresponds to graphene-like regions that give rise to the weak spots in the diffraction pattern of Figure 2c. Similar images from the same area were obtained when the defocusing value was changed in the TEM. Therefore, Figure 2d also demonstrates the presence of graphite- or graphene-like sheets embedded in the Ag lattice.

The above structural information was corroborated by computer image simulations of the HRTEM images. The simulated image, Figure 2e displays tetragonal symmetry as expected from the projection of Ag along the $[11\bar{2}]$ direction. This image is superimposed on a magnified image of the bottom rectangle in Figure 2d. Very similar images with tetragonal symmetry were obtained for a series of defocusing values, $-47.37 \text{ nm} \leq \Delta f \leq -35.70 \text{ nm}$ and thicknesses $0.25 \text{ nm} \leq t \leq 2.25 \text{ nm}$ which agreed with HRTEM images obtained under these imaging conditions. The regions with hexagonal symmetry in the upper rectangle in Figure 2d are in agreement with simulated images from graphene along the [0001] direction displayed as inset to Figure 2f and superimposed on a magnified image of the top rectangle in Figure 2d. Simulated images of graphite under the same imaging conditions showed the opposite contrast to that observed in Figure 2f. Therefore, carbon incorporates in this region of the sample in the form of a graphene-like sheet or ribbon with an epitaxial relation with the Ag lattice of (0001) graphene//$(11\bar{2})$ Ag and $[11\bar{2}0]$ graphene//$[1\bar{1}0]$ Ag.

3. Carbon with sp^2 Bonding in Ag Covetic

The Ag cv 6% and pure Ag samples were investigated using Raman spectroscopy, and the presence of infused graphitic carbon in Ag covetic is confirmed by the Raman spectrum in **Figure 3**a which shows the characteristic D and G peaks of graphitic sp^2 bonding at ≈1333 and ≈1600 cm^{-1}, respectively,[27] compared to a pure Ag metal sample in Figure 3c. Spectra were taken at 20 points along a line of Ag covetic (Figure 3b) and 22 points in the Ag metal sample (Figure 3d) with exactly the same parameters and laser power intensity as indicated in the Experimental Section.

Raman spectra from nominally pure (99.99%) Ag (Figure 3c,d) show weak and broad peaks at 240, 1120, 1395, and 1587 cm^{-1}, although in general, the intensities are quite low since laser power had to be minimized on the Ag surface as Ag is highly prone to photodecomposition (again, we highlight that the same Raman acquisition settings were used on both Ag and Ag covetic samples). The peaks at 240 and 1120 cm^{-1} can be assigned to Ag–O and Ag–S stretching and bending modes,[28] while the bands at 1395 and 1587 cm^{-1} are attributed to adsorbed carbon species, either from contamination or the polishing process. The 1395 cm^{-1} has contributions from CH_n hydrocarbons and from the disorder band that is assigned to graphite (D band). The 1587 cm^{-1} peak can also be assigned to graphitic species (G band). Finally, the peak at ≈2900 cm^{-1} can be assigned to C–H vibrational stretching in aliphatic alkanes.[28] Although both (pure Ag and Ag covetic) samples show the presence of graphitic carbon, these signals were not observed in all 22 point scans in the pure metal (Figure 3d). Furthermore, the intensities of these peaks, when observed on the pure Ag surfaces, are roughly two orders of magnitude lower than the corresponding Ag covetic sample (Figure 3b). Moreover, silver surfaces have an enhancement factor, and on previous calculations,[29] the actual carbonaceous impurities are likely confined to the surface, well below complete coverage.

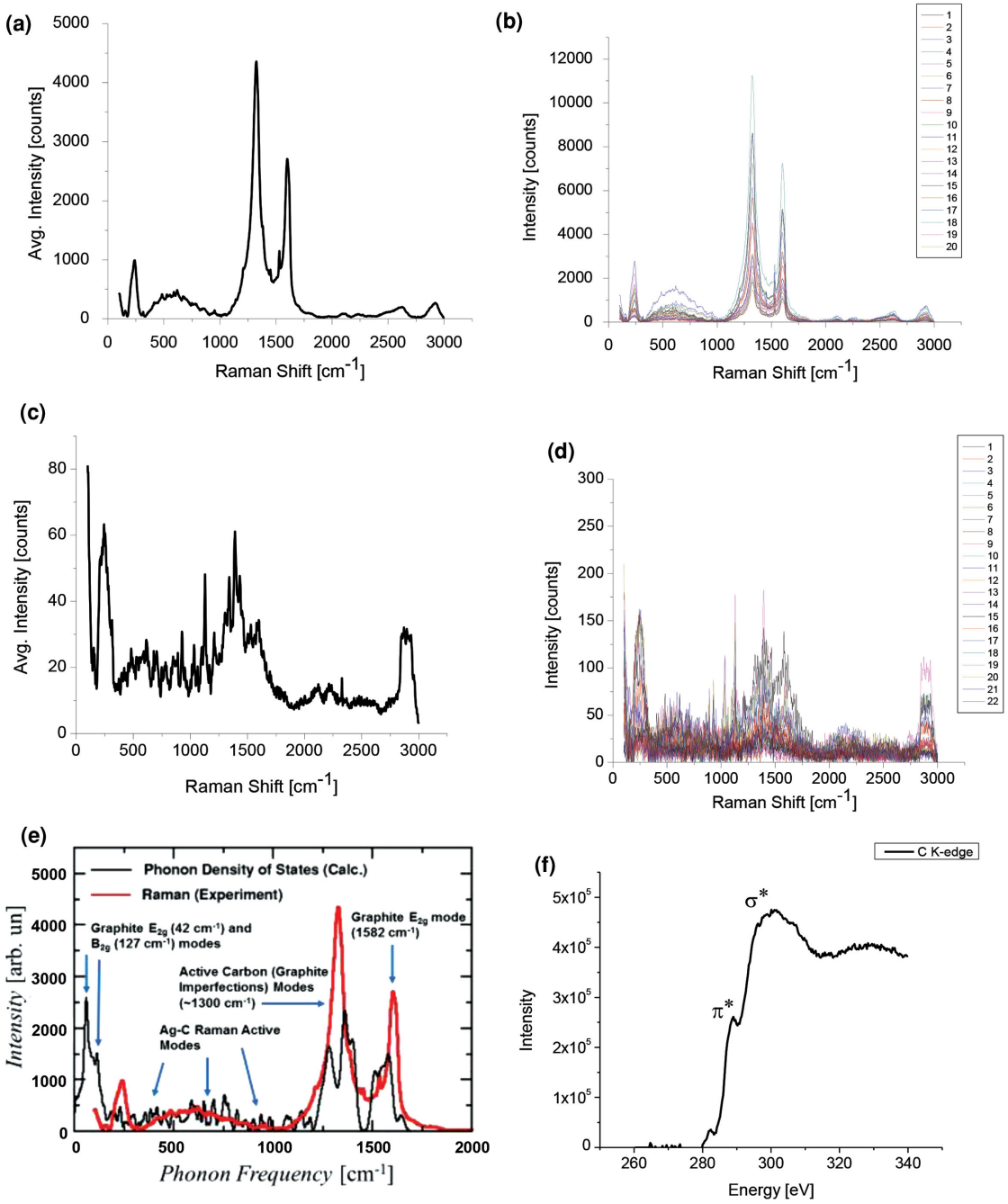

Figure 3. a) Average Raman spectrum and b) individual spectra obtained at 20 different points of an Ag cv 6% sample. c) Average Raman spectrum and (d) individual spectra from 22 different points of an Ag metal sample obtained with the same parameters as (a). The individual spectra in (b) and (d) are displaced vertically for clarity. e) Raman spectrum from Ag cv 6% and phonon density of states calculated by the DFT-based approach. All Raman spectra were taken with a laser excitation wavelength of 632 nm. f) Electron energy loss spectrum of the C-K edge in Ag cv 3%. The π^* and σ^* edges are characteristic of sp^2 bonding.

On the other hand, the covetic sample shows strong D and G peaks in all 20 points (Figure 3b). The G-band at ≈1601 cm^{-1} in the average spectrum in Figure 3a, with variation from 1596 to 1604 cm^{-1} in the 20 points in Figure 3b, corresponds to the E_{2g} mode at the BZ center of nanocrystalline graphite.[30] The G-band is typically located at 1540 to 1600 cm^{-1}. In the present case, the G-band at 1601 cm^{-1} is highly indicative of not only having highly ordered carbon species infused into the metal, but also a high ratio of sp^2 to sp^3 bonding and high strain.[30,31] The D band at 1334 cm^{-1}, normally in the range 1300–1400 cm^{-1}, corresponds to defects and is active in defective graphite, amorphous carbon, carbon nanotubes, and graphene but is not observed in perfect graphite or diamond.[32] The peak at 2625 cm^{-1} in the covetic sample corresponds to the G′ overtone of the D

mode of graphite. First-principles DFT based calculations of the dynamic matrix and corresponding phonon spectrum for different supercells (see Section 5) allow accurate identification and interpretation of the vibration modes of the system. In particular, we found that the bonds between Ag and C atoms at graphene sheet defects (such as vacancies and edges) are responsible for the broad peak between 300 and 1000 cm^{-1} in the Raman spectrum (Figure 3e). The Raman data corroborate the presence of graphitic-like regions in the Ag covetic with primarily sp^2 bonding but with high density of defects and strain.

The sp^2 bonding of carbon in covetics is also evident in the shape of the C 1s XPS spectrum, Figure 1c, which displays an asymmetric peak at 284.4 eV indicative of sp^2 C bonding.[33] The FWHM of 2.52 eV of this peak is higher than 1.12 eV typically observed in graphite[33] indicating the presence of more than one bonding phase. Carbon with sp^3 bonding has a C 1s peak at 290 eV which is not observed in Figure 1c although there is a tail in the high energy range for the peak at 284.4 eV. Evidence for sp^2 bonding of C is also obtained from the electron energy loss spectrum of the C-K edge in Ag cv 3% in Figure 3f which displays a sharp edge at 284 eV corresponding to transitions of the C 1s electron to π^* antibonding unoccupied orbital in graphitic carbon.[34] This signal is only observed in carbon having sp^2 bonding. The feature at ≈290 eV corresponds to transitions to the σ^* level in carbon and is observed in all carbon allotropes.[34] The edge at 284 eV is not as sharp as it would be in graphite. However, the ratio of the integrated intensity of the π^* to that of the σ^* edges $I(\pi^*)/I(\sigma^*) = 0.54$ in Ag cv 3% compared to 0.46 obtained from activated carbon (not shown) indicates that the graphite-like regions in Ag covetic while defective have for the most part sp^2 bonding. Thus, carbon in silver covetic has sp^2 bonding, and forms graphene-like sheets with 3D nano-epitaxial relation with the silver lattice.

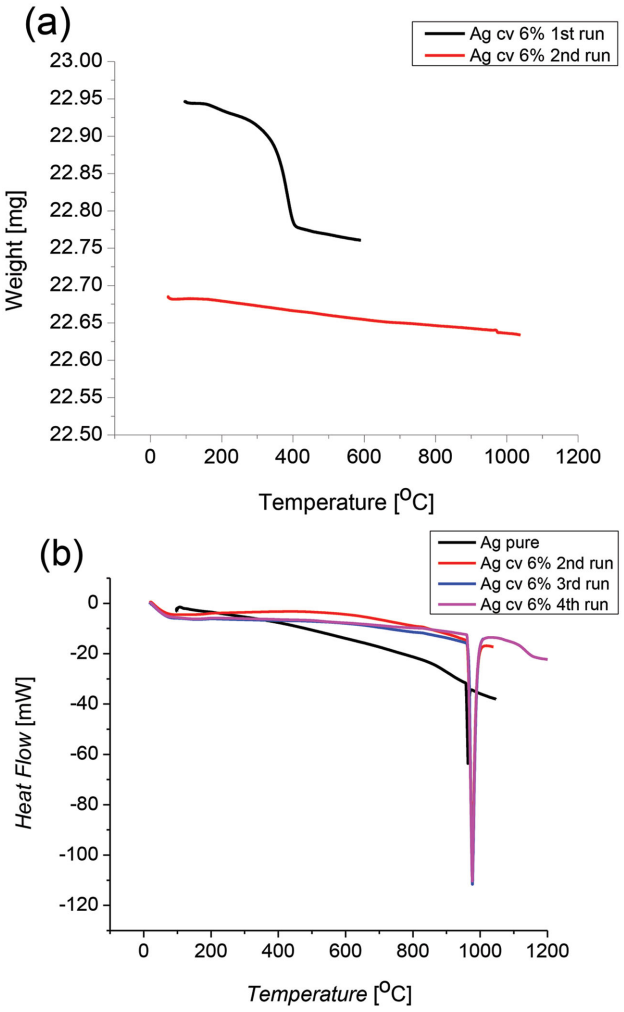

Figure 4. a) Thermogravimetric analysis (TGA) graph from Ag cv 6% on heating first to 600 °C and a second time to 1020 °C. Some unincorporated carbon oxidizes or decomposes from the sample during the first heating run starting at ≈200 °C. No weight reduction was observed in the second heating cycle. b) Differential scanning calorimetry (DSC) graph at a heating rate of 20 °C min^{-1} obtained during the second, third, and fourth heating cycles from Ag cv 6%. The melting temperature is 976.5 °C. The black curve in (b) corresponds to 99.99% pure Ag metal.

4. Thermal Stability of Ag Covetic

Carbon incorporation in silver covetic has high thermal stability and increases the melting temperature of the material to 976.5 °C for Ag cv 6% compared to 961.78 °C for pure Ag metal, **Figure 4**. In the first run an Ag cv 6% sample was heated to 600 °C in order to promote decomposition of any carbon that was not incorporated in the silver lattice. This is evidenced in Figure 4a by the loss of weight starting at ≈200 °C during the first heating run. In the second heating experiment to 1020 °C there was minimal weight loss of the sample (Figure 4a) and the differential scanning calorimetry curve, Figure 4b, indicates a melting temperature of 976.5 °C (≈15° above the melting temperature of silver). Two additional heating cycles showed no further decrease in weight and the same melting temperature of 976.5 °C (Figure 4b). Hence, the remaining carbon in the silver covetic sample did not phase separate upon repeated melting and resolidification, strengthening the assertion that Ag covetic is a stable material with a high energy Ag—C bond. The calculated enthalpy of fusion for Ag covetic is $\Delta H_m = 8.71$ kJ mol^{-1} compared to 11.3 kJ mol^{-1} for Ag indicating that it takes higher temperature to melt Ag covetic but once this temperature is achieved less energy is required to melt the material compared to Ag metal. Hence, Ag covetic and Ag metal have a different melting temperature and the Ag and C remain bonded in the molten covetic phase.

5. Bonding Interactions

Despite the uneven distribution of the 3D epitaxial structures of the nanocarbon in the silver crystalline lattice in Ag covetics, the results presented here indicate that this material is highly stable. Furthermore, this electrocharging assisted bulk process of introducing C in metals is an alternative process that could solve the problem of oxidation of Ag in air especially for nanostructures and thin films.[1,2,35] The stability of Ag covetic is probably a result of strong bonding between the C and the Ag as we obtained from theoretical models using density functional theory (DFT) for a 3D epitaxial structure of graphene

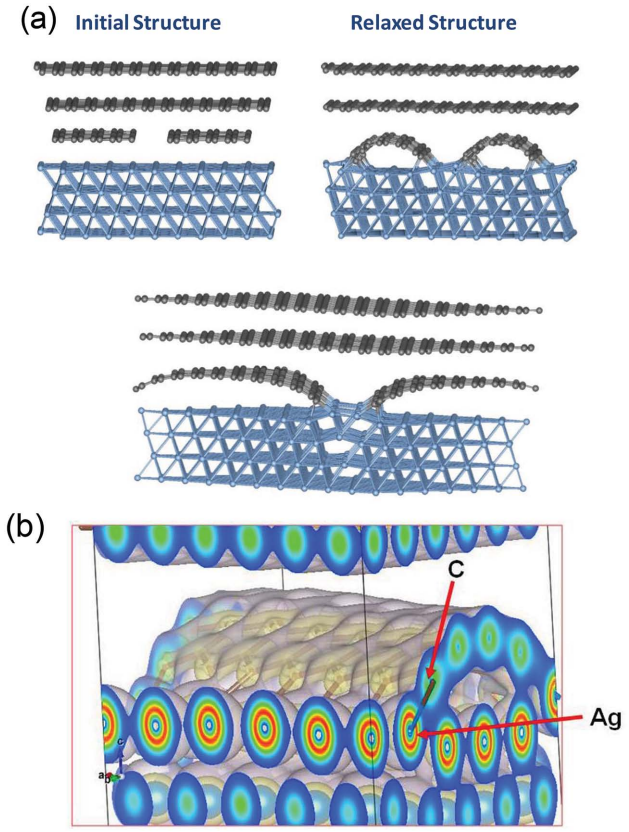

Figure 5. a) DFT simulations for a structure of graphene/silver interface with a narrow width before and after relaxation (top) and wider width (bottom) ribbons bonding to Ag neighboring plane. The bending of the graphene ribbons is reduced as the width of the ribbons increases. Bonding between Ag and C occurs at the edges of the ribbons. b) DFT calculations of the electron density showing the bond between C and Ag at the edges of the graphene-like ribbon.

and Ag (111) planes which show that if the graphene is perfect there is no bonding between Ag and C. This is not surprising since in perfect graphene all the C atoms have saturated bonds. It should be noted that π-bonding from graphene to metal *d*-orbitals is usually observed when a metal is vapor deposited onto graphene.[36] However, our DFT calculations indicate that direct bonding between C and Ag in covetics is possible whenever there are C vacancies in the graphene layer and/or at edges of graphene sheets, i.e., undercoordinated C atoms in graphene bond to Ag atoms from the neighboring plane. **Figure 5**a shows that bonding between C and Ag takes place at the edges of graphene-like ribbons. Our DFT calculations show that the bonds between C and Ag are covalent with bonding energies in the range 1.2–2.2 eV per graphene vacancy and/or per atom at the edge of a ribbon. Furthermore, the bonds between Ag and C atoms at vacancies and edges are responsible for the broad peak in the Raman spectrum of Ag cv 6% (Figure 3e). Namely, first principles calculations of the dynamic matrix and corresponding phonon spectrum for the supercells used in the DFT calculations shown in Figure 5 as well as eigenvectors and eigenvalues for all the phonons allow identification and interpretation of the vibration modes of the system. Figure 3e shows that in addition to "pristine" graphite modes (at 127 and 1582 cm^{-1}) related to the vibrations of sp^2 bonded carbon atoms in graphite layers, and to defect graphite modes (at ≈1300 cm^{-1}) related to the graphite layer defects (e.g., edges of graphene sheets) and sheet bending (see Figure 5a), we have a broad hump in the Raman spectrum of the Ag covetic (the hump is absent in pure Ag) between 300 and 1000 cm^{-1}. Analysis of the dynamic matrix for these phonons indicates that these vibration modes are related to the Ag—C bonds which have covalent character (see Figure 3e). The DFT-based analysis of electron density indicates that Ag and C form common covalent electron orbital (see Figure 5b). The bond between C and Ag should give rise to a peak in the low energy range of the C 1s and Ag 3d peaks in the XPS spectrum of the covetic sample. However, no such peaks are observed (Figure 1c). Since bonding between C and Ag only takes place at edges of the graphene sheets and wherever there is a C vacancy the contribution from Ag—C bonding to the XPS peaks would be very weak given that the area under the peak is proportional to the concentration.

6. Conductivity of Ag Covetic

The relatively high C concentration observed in Ag covetic is expected to play a role on the properties of the material. At room temperature, for example, we measured a resistivity of Ag covetic of $\rho = 1.78 \times 10^{-6}$ Ω cm (conductivity, $\sigma = 5.62 \times 10^{7}$ S m^{-1}) compared to $\rho = 1.58 \times 10^{-6}$ Ω cm ($\sigma = 6.2 \times 10^{7}$ S m^{-1}) for pure Ag, i.e., the conductivity of Ag covetic is 91% that of pure Ag even with ≈6 wt% (36.4 at%) C and more than two orders of magnitude higher than that of Ag/CNT and Ag@CNT composites.[37] It is possible that better control of the C incorporation in the Ag lattice would increase the electrical conductivity of Ag covetic even further.

7. Conclusions

Covetics are alloys of metals with high carbon content in which the carbon is incorporated via electrocharging assisted bulk processing technique. Our results show that Ag covetic contains C in much higher concentrations than had ever been possible to achieve in silver by traditional methods. This material is very stable, can be remelted and resolidified without the carbon separating from the metal. Nanocarbon forms graphene-like regions in a 3D nanoepitaxy embedded in the lattice of Ag forming a new structure. DFT calculations indicate that C and Ag form covalent bonds at the edges of the graphitic-like sheets and at vacancies. The conductivity of Ag covetic with ≈6 wt% (36.4 at%) C at room temperature exhibits ≈90% of the conductivity of 99.99% pure Ag and much higher than composites of Ag and CNT. Our results lay ground work for these materials and open up whole new areas of fundamental and applied investigations regarding basic covetic properties as well as unforeseen device applications based on the properties observed in this initial work. Nanostructures based on Ag covetic and other covetic materials, such as Cu- and Al-covetic, still need to be investigated. Furthermore, the actual process of C incorporation in the crystalline lattice of the metal host upon conversion to covetics still needs to be unraveled to gain

fundamental understanding of their physical and chemical properties so that new materials can be designed with specific properties.

8. Experimental Section

Ag covetic with 3 wt% (21.74 at%) and 6 wt% (36.44 at%) C was received from Third Millennium Materials, LLC, Waverly, OH. The as-received samples were cut into small pieces and polished with diamond paper with particle size starting with 30 μm followed by 15, 9, 3, 1, and 0.25 μm to remove any surface contamination during conversion process and any scratches from the saw used to cut the samples. After polishing, the samples were cleaned with acetone and placed in an ultra sonicator in methanol and isopropyl alcohol to remove any diamond particles left from the polishing paper and any residual surface contamination. Samples were characterized by scanning electron microscopy using a Hitachi Su-70 field emission SEM with an energy dispersive X-ray spectrometer Bruker Si drift detector (SDD) and spatial resolution of 1 nm. The samples for transmission electron microscopy (TEM) were prepared by mechanical polishing with diamond paper with decreasing particle size down to a thickness of ≈30 μm followed by Ar^+ ion milling. TEM observation was carried out in a JEOL 2100F field emission TEM operated at 200 kV with a spherical aberration coefficient of C_s = 0.5 mm, point–point resolution of 0.19 nm and lattice resolution of 0.10 nm. The JEMS software version 3.8431U2012 was used for computer image simulation of the TEM high resolution lattice images. XPS data were collected with Mg X-rays (1287 eV) using Physical Electronics Model 5400 spectrometer. Survey spectra were collected at constant pass energy of 89.5 eV. Multiplex spectra were collected at constant pass energy of 35.8 eV and an electron takeoff angle of 45°. The area analyzed by XPS was a spot with a diameter of 1.1 mm. Depth profiling was done with 4 keV Ar-ions using a rastered area of 5 × 5 mm with an estimated sputtering rate of ≈2 nm of SiO_2 per minute. The local atomic structure for Ag covetic was also examined using X-ray absorption spectroscopy (XAS). The XAS experiments were conducted on the bending magnet station X-19A of the National Synchrotron Light Source with the electron storage ring operating at electron energy of 2.8 GeV and a stored current near 250 mA. The XAS spectra at the Ag L_3-edge (3351 eV) were collected in the fluorescence mode at room temperature using a double-crystal monochromator with two flat Si (111) crystals detuned by 60% to reduce the harmonic-content of the beam. The XANES and EXAFS spectra were not corrected for self-absorption by the sample. X-ray powder diffraction spectra of bulk Ag covetics were measured on a Bruker D8 Advance powder diffractometer using CuKα radiation from a sealed tube, Ni β-filter, 0.25 mm incident and diffracted beam Soller slits, and LynxEye position sensitive detector. The spectra were measured from 30° to 145° 2θ with step of 0.0145°, and 1 s exposure. Full fitting of the spectra was performed using the Rietveld method. Since the data were collected from bulk samples it was necessary to account for preferred orientation and anisotropy in peak asymmetry, anisotropy in peak broadening and shift due to crystallite size and strain which was done in spherical harmonic approach using TOPAS-4 software (Bruker).

Raman spectra were obtained using an integrated confocal micro-Raman system (Yvon Jobin LabRAM ARAMIS) equipped with two internal lasers as excitation wavelength source: Nd:YAG (532 nm) and HeNe (632.8 nm). Measurements were performed using radiation at 632.8 nm with a real output power of 9 mW. A filter was used to modulate the laser power on the samples by a factor of 0.1. The Olympus BX41 microscope is equipped with Leitz objectives of 10×, 50×, and 100×. The samples were observed with the 10× objective, which gives a laser spot of 3.09 μm. The analyzed areas were pinpointed by using a TV camera attached to the microscope. 20 point map on a 300 μm line was surveyed 2× using 600 grating for 6 s.

TGA/DSC data were obtained using a SDT Q600 from TA Instruments. Data were collected at a temperature rate of 20 °C min^{-1}. The sample was covered under an atmosphere of Ar gas with flow rate of 90 mL min^{-1}. The crucible for the TGA/DSC was an alumina pan. The initial covetic sample weighted 55 mg. Resistivity measurements were carried out in a Quantum Design Physical Properties Measurement System (PPMS) using a standard four-probe arrangement of silver paste contacts with gold wire leads.

In order to investigate the role of different atomic scale and nanoscale features in the epitaxial accommodation of graphene layers and graphene ribbons at the Ag surfaces and between layers with [111] orientation, a significant number of different graphene–Ag periodic supercells was constructed and their geometries optimized using DFT. In particular, two types of supercells were used: i) "bulk" supercells with alternating Ag [111] and graphene layers (typically, they consisted of three layers of Ag and three layers of graphene); ii) "slab" supercells (three layers of graphene on top of three layers of Ag [111]) and free surface. For alternating layers a periodic hexagonal supercell with parameters a = 1.446 nm; c = 1.786 nm was used. The value of the parameter a corresponds to ≈5 lattice constants of the 2D periodic structure in Ag (111) plane and ≈6 lattice constants of the graphene structure, i.e., to account for the lattice mismatch between these two structures. For slab supercells a vacuum layer was added between slabs of ≈1.4 nm in the c direction which guarantees that different slabs will not overlap. The positions of Ag atoms in the lower layer of the slab (opposite to the "free" graphene surface) were fixed.

The calculations were based on the generalized gradient approximation (GGA) for exchange and correlation, and plane waves.[38] The GGA functional of Perdew, Burke, and Ernzerhof (PBE)[39] was used, which gives good results for chemisorption of molecules at transition-metal surfaces. Projected augmented wave (PAW) scalar relativistic pseudopotentials,[40] and the VASP code[41] were used. The energy cutoff for the plane-wave basis was set at 500 eV, and all integrations over the Brillouin zone were done using the Monkhorst–Pack scheme with one to four k points in the relevant irreducible wedge.[42] Inclusion of additional k points was found to have minimal effect on the total-energy differences of interest. The total number of atoms varied between 300 and 500 atoms for different periodic supercells. For each supercell, all atoms were relaxed until the quantum-mechanical force on each atom became smaller than 0.02 eV $Å^{-1}$. Most of the calculations were spin-polarized. Activation barriers were calculated using the nudged-elastic-band (NEB) method.[43] In some cases (when the potential energy curve was very steep around the transition state) the adaptive NEB approach was employed,[44] because the conventional NEB sampling did not provide satisfactory results. The pre-exponential factors and reaction rates were not calculated for the considered reactions. Although such calculations could be performed,[45] they are very difficult and time consuming. Comparison between the activation barriers at different surface sites provides only qualitative information which, however, is quite sufficient for most of the practical purposes.

Supporting Information

Supporting Information is available from the Wiley Online Library or from the author.

Acknowledgements

This work was supported in part by DARPA/ARL under Contract No. W911NF13100, ONR under Contract No. N000141410042, the University of Maryland Faculty Incentives Program. The authors acknowledge the NISP laboratory at the University of Maryland for the use of the microscopy facilities. The Ag covetic samples were provided by Third Millennium Materials, LLC. A.N.M. acknowledges financial support by the Carderock Division of the Naval Surface Warfare Center's In-house Laboratory Independent Research Program administrated under ONR's Program Element 0601152N. The XAS experiments were conducted at the National Synchrotron Light Source of Brookhaven National

Laboratory, which is supported by the U.S. Department of Energy, Office of Basic Energy Sciences, under Contract No. DE-AC02–98CH10886. Ab initio calculations were performed by using DOE NERSC resources (Contract DEAC02- 05CH11231). M.M.K. is grateful to the Office of the Director of NSF for support under the IRD program. Any appearance of findings, conclusions, or recommendations expressed in this manuscript are those of the authors and do not necessarily reflect the views of NSF.

Received: March 22, 2015
Revised: May 21, 2015
Published online: July 2, 2015

[1] *Nature* **1951**, *168*, 639.
[2] J. L. Elechiguerra, L. Larios-Lopez, C. Liu, D. Garcia-Gutierrez, A. Camacho-Bragado, M. J. Yacaman, *Chem. Mater.* **2005**, *17*, 6042.
[3] H. E. Bennett, R. L. Peck, D. K. Burge, J. M. Bennett, *J. Appl. Phys.* **1969**, *40*, 3351.
[4] a) I. Karakaya, W. T. Thompson, *Bull. Alloy Phase Diagrams* **1988**, *9*, 226; b) H. Okamoto, T. B. Massalski, *Bull. Alloy Phase Diagrams* **1984**, *5*, 378; c) B. Predel, *C–Cu (Carbon–Copper) Binary Phase Diagram*, Springer Materials.
[5] T. Knych, P. Kwasniewski, G. Kiesiewicz, A. Mamala, A. Kawecki, B. Smyrak, *Metall. Mater. Trans. B* **2014**, *45*, 1196.
[6] K. S. Novoselov, A. K. Geim, S. V. Morozov, D. Jiang, Y. Zhang, S. V. Dubonos, I. V. Grigorieva, A. A. Firsov, *Science* **2004**, *306*, 666.
[7] S. Iijima, *Nature* **1991**, *354*, 56.
[8] S. Bae, H. Kim, Y. Lee, X. Xu, J.-S. Park, Y. Zheng, J. Balakrishnan, T. Lei, H. R. Kim, Y. I. Song, Y.-J. Kim, K. S. Kim, B. Ozyilmaz, J.-H. Ahn, B. H. Hong, S. Iijima, *Nat. Nanotechnol.* **2010**, *5*, 574.
[9] I. Forbeaux, J. M. Themlin, J. M. Debever, *Phys. Rev. B* **1998**, *58*, 16396.
[10] D. C. Marcano, D. V. Kosynkin, J. M. Berlin, A. Sinitskii, Z. Sun, A. Slesarev, L. B. Alemany, W. Lu, J. M. Tour, *ACS Nano* **2010**, *4*, 4806.
[11] K. R. Paton, E. Varrla, C. Backes, R. J. Smith, U. Khan, A. O'Neill, C. Boland, M. Lotya, O. M. Istrate, P. King, T. Higgins, S. Barwich, P. May, P. Puczkarski, I. Ahmed, M. Moebius, H. Pettersson, E. Long, J. Coelho, S. E. O'Brien, E. K. McGuire, B. M. Sanchez, G. S. Duesberg, N. McEvoy, T. J. Pennycook, C. Downing, A. Crossley, V. Nicolosi, J. N. Coleman, *Nat. Mater.* **2014**, *13*, 624.
[12] a) J. C. Reed, H. Zhu, A. Y. Zhu, C. Li, E. Cubukcu, *Nano Lett.* **2012**, *12*, 4090; b) H.-W. Tien, S.-T. Hsiao, W.-H. Liao, Y.-H. Yu, F.-C. Lin, Y.-S. Wang, S.-M. Li, C.-C. M. Ma, *Carbon* **2013**, *58*, 198; c) J. Chen, H. Bi, S. Sun, Y. Tang, W. Zhao, T. Lin, D. Wan, F. Huang, X. Zhou, X. Xie, M. Jiang, *ACS Appl. Mater. Interfaces* **2013**, *5*, 1408; d) X. S. Li, W. W. Cai, J. H. An, S. Kim, J. Nah, D. X. Yang, R. Piner, A. Velamakanni, I. Jung, E. Tutuc, S. K. Banerjee, L. Colombo, R. S. Ruoff, *Science* **2009**, *324*, 1312.
[13] a) P. C. Ma, B. Z. Tang, J.-K. Kim, *Carbon* **2008**, *46*, 1497; b) S. B. Menzel, J. Thomas, U. Weissker, F. Schaffel, C. Hossbach, M. Albert, S. Hampel, T. Gemming, *J. Nanosci. Nanotechnol.* **2009**, *9*, 6096.
[14] C. Subramaniam, T. Yamada, K. Kobashi, A. Sekiguchi, D. N. Futaba, M. Yumura, K. Hata, *Nat. Commun.* **2013**, *4*, 2202.
[15] Y. Kim, J. Lee, M. S. Yeom, J. W. Shin, H. Kim, Y. Cui, J. W. Kysar, J. Hone, Y. Jung, S. Jeon, S. M. Han, *Nat. Commun.* **2013**, *4*, 2114.
[16] J. V. Shugart, R. C. Scherer, *USA Patent 8349759*, **2013**.
[17] a) H. Mehrer, *Diffusion in Solids: Fundamentals, Methods, Materials, Diffusion-Controlled Processes*, Springer, Berlin **2007**; b) H. B. Huntington, *Electromigration in Metals*, Academic Press, New York **1975**.
[18] Y.-i. Kim, E. Nishikawas, T. Kioka, *J. Plasma Fusion Res.* **2009**, *8*, 612.
[19] R. Borgohain, J. Yang, J. P. Selegue, D. Y. Kim, *Carbon* **2014**, *66*, 272.
[20] JCPDS 89–3840.
[21] T. Blanton, S. Misture, N. Dontula, S. Zdzieszynski, *Powder Diffr.* **2011**, *26*, 114.
[22] a) C. Lee, X. Wei, J. W. Kysar, J. Hone, *Science* **2008**, *321*, 385; b) M. Poot, H. S. J. van der Zant, *Appl. Phys. Lett.* **2008**, *92*.
[23] D. Yoon, Y.-W. Son, H. Cheong, *Nano Lett.* **2011**, *11*, 3227.
[24] W. Bao, F. Miao, Z. Chen, H. Zhang, W. Jang, C. Dames, C. N. Lau, *Nat. Nanotechnol.* **2009**, *4*, 562.
[25] S. Linas, Y. Magnin, B. Poinsot, O. Boisron, G. D. Foerster, V. Martinez, R. Fulcrand, F. Tournus, V. Dupuis, F. Rabilloud, L. Bardotti, Z. Han, D. Kalita, V. Bouchiat, F. Calvo, *Phys. Rev. B* **2015**, *91*.
[26] K. V. Zakharchenko, J. H. Los, M. I. Katsnelson, A. Fasolino, *Phys. Rev. B* **2010**, *81*.
[27] A. C. Ferrari, *Solid State Commun.* **2007**, *143*, 47.
[28] I. Martina, R. Wiesinger, M. Schreiner, *J. Raman Spectrosc.* **2013**, *44*, 770.
[29] J. C. Tsang, J. E. Demuth, P. N. Sanda, J. R. Kirtley, *Chem. Phys. Lett.* **1980**, *76*, 54.
[30] A. C. Ferrari, J. Robertson, *Phys. Rev. B* **2000**, *61*, 14095.
[31] J. Wagner, M. Ramsteiner, C. Wild, P. Koidl, *Phys. Rev. B* **1989**, *40*, 1817.
[32] M. S. Dresselhaus, G. Dresselhaus, R. Saito, A. Jorio, *Phys. Rep.* **2005**, *409*, 47.
[33] J. C. Lascovich, R. Giorgi, S. Scaglione, *Appl. Surf. Sci.* **1991**, *47*, 17.
[34] R. F. Egerton, M. J. Whelan, *J. Electron Spectrosc. Relat. Phenom.* **1974**, *3*, 232.
[35] a) H. Masuda, T. Kizuka, *Jpn. J. Appl. Phys.* **2010**, *49*; b) L. Hu, H. Wu, Y. Cui, *MRS Bull.* **2011**, *36*, 760.
[36] B. J. Schultz, C. Jaye, P. S. Lysaght, D. A. Fischer, D. Prendergast, S. Banerjee, *Chem. Sci.* **2013**, *4*, 494.
[37] a) R. K. Agrawalla, S. Paul, P. K. Sahoo, A. K. Chakraborty, A. K. Mitra, *J. Appl. Polym. Sci.* **2015**, *132*; b) K.-Y. Chun, Y. Oh, J. Rho, J.-H. Ahn, Y.-J. Kim, H. R. Choi, S. Baik, *Nat. Nanotechnol.* **2010**, *5*, 853.
[38] M. C. Payne, M. P. Teter, D. C. Allan, T. A. Arias, J. D. Joannopoulos, *Rev. Mod. Phys.* **1992**, *64*, 1045.
[39] J. P. Perdew, K. Burke, M. Ernzerhof, *Phys. Rev. Lett.* **1996**, *77*, 3865.
[40] a) P. E. Blochl, *Phys. Rev. B* **1994**, *50*, 17953; b) G. Kresse, D. Joubert, *Phys. Rev. B* **1999**, *59*, 1758.
[41] a) G. Kresse, J. Hafner, *Phys. Rev. B* **1993**, *48*, 13115; b) G. Kresse, J. Furthmuller, *Phys. Rev. B* **1996**, *54*, 11169.
[42] D. J. Chadi, M. L. Cohen, *Phys. Rev. B* **1973**, *8*, 5747.
[43] H. Jonsson, G. Mills, K. W. Jacobsen, World Scientific, Singapore **1998**, p. 385.
[44] P. Maragakis, S. A. Andreev, Y. Brumer, D. R. Reichman, E. Kaxiras, *J. Chem. Phys.* **2002**, *117*, 4651.
[45] O. Sharia, M. M. Kuklja, *J. Phys. Chem. C* **2012**, *116*, 11077.